Physics of Fluids

Numerical instability investigation of inward radial Rayleigh–Bénard–Poiseuille flow

Cite as: Phys. Fluids **33**, 034120 (2021); https://doi.org/10.1063/5.0043823
Submitted: 11 January 2021 . Accepted: 22 February 2021 . Published Online: 19 March 2021

M. K. Hasan, and A. Gross

Physics of Fluids ARTICLE scitation.org/journal/phf

Numerical instability investigation of inward radial Rayleigh–Bénard–Poiseuille flow

Cite as: Phys. Fluids 33, 034120 (2021); doi: 10.1063/5.0043823
Submitted: 11 January 2021 · Accepted: 22 February 2021 ·
Published Online: 19 March 2021

M. K. Hasan[a] and A. Gross

AFFILIATIONS

Mechanical and Aerospace Engineering Department, New Mexico State University, Las Cruces, New Mexico 88003, USA

[a]Author to whom correspondence should be addressed: kamrul04@nmsu.edu

ABSTRACT

The spatial instability of inward radial Rayleigh–Bénard–Poiseuille flow was investigated using direct numerical simulations with random and controlled inflow forcing. The simulations were carried out with a higher-order-accurate compact finite difference code in cylindrical coordinates. Inward radial Rayleigh–Bénard–Poiseuille flows can be found, for example, in the collectors of solar chimney power plants. The conditions for the present simulations were chosen such that both steady and unsteady three-dimensional waves are amplified. The spatial growth rates are attenuated significantly in the downstream direction as a result of strong streamwise acceleration. For the oblique waves, the growth rates and wave angles decrease and the phase speeds get larger with increasing frequency. As the oblique waves travel downstream, the phase speeds decrease and the wave angles increase. Overall, steady waves with a wave angle of 90° are the most amplified. In general, because of the finite azimuthal extent, only certain azimuthal wavenumbers are possible. As a result, the steady waves appear to merge in the streamwise direction. When the inflow is at an angle such that a spiral flow is formed, one family of oblique waves is favored over the other and the mode shapes of the left- and right-traveling oblique waves are asymmetric with respect to the radius. As the inflow angle increases, this asymmetry is aggravated and the wavenumber of the most amplified disturbances is diminished.

I. INTRODUCTION

The radial channel flow between two horizontal and circular parallel plates with the temperature gradient in the wall-normal direction and opposing gravitational field is known as radial Rayleigh–Bénard–Poiseuille (RBP) flow as opposed to plane RBP flow. Because of the geometric configuration, two types of flows are possible, which are inward and outward radial RBP flow. Inward radial RBP flows, for example, are found in the collectors of solar chimney power plants (SCPPs). Both inward and outward RBP flow can exhibit buoyancy-driven instability. Two non-dimensional numbers, namely, the Reynolds number,

$$Re = \frac{u_{max} h/2}{\nu}, \tag{1}$$

with u_{max} being the maximum velocity, h being the channel height, and ν being the kinematic viscosity, and the Rayleigh number,

$$Ra = \frac{g h^3 \gamma \Delta T}{\nu \alpha}, \tag{2}$$

with g being gravitational acceleration, γ being the volumetric thermal expansion coefficient, ΔT being the temperature difference, and α being the thermal diffusivity, govern the onset of flow instability.

The hydrodynamic instability of plane RBP flow has been the focus of much research because of its many scientific and engineering applications. Linear stability investigations of plane RBP flow by Gage and Reid[1] provided neutral curves (stability boundaries) for the onset of both buoyancy- and viscosity-driven instability. According to Gage and Reid,[1] for $Re < Re_c = 5400$ and $Ra > Ra_c = 1708$, buoyancy-driven instability (thermal effect) occurs and three-dimensional (3-D) waves are most amplified. These waves can develop into longitudinal vortices. On the other hand, for $Re > Re_c = 5400$ and $Ra < Ra_c = 1708$, viscosity-driven instability occurs and two-dimensional (2D) waves in the form of Tollmien–Schlichting (T–S) waves are most amplified (the effect of shear is dominant). When the disturbance amplitudes become non-linear, transverse rolls are formed. Later on, Orszag[2] carried out linear temporal stability analyses of plane Poiseuille flow and obtained a more accurate value of the critical Reynolds number for T–S waves, $Re_c = 5772.22$. According to Luijkx *et al.*,[3] for a finite aspect ratio channel, transverse rolls can appear first below the critical Reynolds number when the Rayleigh number is above the critical value. However, 3D longitudinal rolls were found when the Reynolds number was increased. A 2D numerical investigation of Poiseuille–Bénard flow in a plane channel by Nicolas *et al.*[4] revealed transverse rolls that were superimposed on the

mean flow. Nicolas *et al.*[5] provided an extensive literature review and employed linear stability theory and numerical analyses for investigating both the primary and secondary instabilities of plane RBP flow. In their finite aspect ratio simulations, longitudinal rolls appeared first near the lateral walls. A correlation was proposed for the "growth length" (i.e., downstream distance from inflow to emergence of fully developed longitudinal rolls) based on the Rayleigh and Reynolds number and vertical velocity along the channel axis. White noise was then introduced at the inlet to obtain wavy longitudinal rolls. The growth length of the wavy rolls was found to linearly decrease with the logarithm of the forcing amplitude. The onset of mixed instability due to the combined effect of buoyancy- and viscosity-driven instability was investigated by Fujimura and Kelly[6] and Ng and Reid.[7] Experiments by Mori and Uchida[8] confirmed the formation of longitudinal rolls when the wall-normal temperature gradient exceeded a critical value. In plane RBP flow experiments by Chang *et al.*,[9,10] the longitudinal flow structures first developed near the channel side walls. Mergui *et al.*[11] carried out both experimental and numerical analyses of plane RBP flow and showed that the boundary layers close to the channel side walls triggered the onset of longitudinal rolls. Hasan and Gross[12] employed temporal direct numerical simulations (DNSs) to investigate the primary buoyancy-driven instability of plane RBP flow in a channel with infinite span. They also found that 3D waves with a wave angle of 90° are most amplified, which corroborates the findings by Gage and Reid.[1] The same authors[13] also investigated the secondary instability of plane RBP flow with longitudinal vortices resulting from a primary buoyancy-driven instability and found a secondary instability that resulted from a triad interaction of the primary steady 3D mode with an unsteady 2D mode and two unsteady oblique modes. In summary, as long as the lateral confinement is negligible and the instability is linear (i.e., modal), longitudinal rolls that are aligned in the streamwise direction will appear first as a result of the primary instability when the Reynolds number is below its critical value and the Rayleigh number is above its critical value.

The hydrodynamic instability of radial RBP has not attracted much attention and is less well understood. This is despite the fact that knowledge of the critical parameters such as the Reynolds number, Rayleigh number, and Prandtl number is of high relevance for the design and operation of engineering applications that feature radial RBP flows such as, for example, SCPPs and chemical vapor deposition (CVD) reactors. Because of continuity ($\rho v \propto 1/r$ relationship), the inward radial flow accelerates strongly in the streamwise direction. Also different from plane RBP flows that have a finite aspect ratio, the aspect ratio is infinite (no sidewall effect). Moreover, since acceleration generally has a stabilizing effect,[14] the stability characteristics of inward radial RBP flow are likely different from those of plane RBP flow.

Fasel *et al.*[15,16] carried out implicit large-eddy simulations and Reynolds averaged Navier–Stokes calculations of the flow through the collector of a 1:33 scale model of the Manzanares SCPP. The simulations revealed both transverse rolls (close to the inlet) and longitudinal vortices (close to the outlet). For the Rayleigh and Reynolds number range of the simulations, longitudinal vortices were expected based on the neutral curves by Gage and Reid.[1] The longitudinal flow structures were reported to enhance the vertical heat transfer in the collector. A direct numerical simulation of the flow inside the collector of the same 1:33 scale SCPP model by Hasan *et al.*[17] revealed strongly amplified steady 3D waves that appear to merge in the downstream direction. The almost step-like mergings were attributed to the fact that only certain azimuthal wavelengths are possible for each radial location. Since the wavelength has to be an integer fraction of the circumference, a continuous smooth adjustment of the wavelength in the streamwise direction is not possible. The natural laminar convection in a radial solar heater was investigated numerically by Bernardes *et al.*[18] The conic chimney geometry was found to affect the mass flow rate and outflow temperature. A numerical investigation of the instability of the inward radial flow between two almost parallel fixed circular plates that resemble the collector of an SCPP was carried out by Bernardes.[19] According to this study, longitudinal vortex structures are formed when the Richardson number, $Ri = Ra/(PrRe^2)$, exceeds 10. Here, $Pr = \nu/\alpha$ is the Prandtl number. Bernardes[20] also developed correlations for the friction factor and Nusselt number (ratio of convective to conductive heat transfer) for flow between two nearly parallel disks. Van Santen *et al.*[21,22] investigated a radial outward flow with buoyancy between two horizontal plates. Transverse rolls were observed for $10 \leq Re \leq 50$ and $Ra = 2000$, which is in disagreement with the study by Gage and Reid.[1] According to Gage and Reid,[1] 3D longitudinal rolls should be unstable for this Reynolds number range and Rayleigh number. When Van Santen *et al.*[21,22] increased the Rayleigh number to $Ra = 5000$, for the same $Re = 50$, torus-shaped flow structures appeared. The relaminarization of turbulent inward radial flow between two fixed parallel disks has been investigated experimentally and numerically by Singh *et al.*[23] The authors examined the effect of acceleration on the flow and found that for a constant Reynolds number, a decrease in the acceleration parameter was observed when the gap ratio (height/radius) was reduced. It was also noticed that decreasing the gap ratio stabilizes the flow.

The dearth of dedicated stability investigations for inward radial RBP flow motivates the present numerical stability analyses. The onset of instability determines if and where flow structures will form. The flow structures will increase the wall-normal momentum and heat transfer. For SCPP applications, this will not only strengthen the heat flux from the ground into the collector but also increase the streamwise pressure drop. For CVD reactor applications, it will affect the uniformity of the deposition. The primary instability of inward radial RBP flow is investigated using direct numerical simulations (DNSs). Different from the earlier temporal stability analyses for plane RBP flow by Hasan and Gross,[12] spatial simulations are employed for the present stability analyses of inward radial RBP flow. First, the Navier–Stokes code and the discretization are described. Next, results from DNS with random unsteady inflow forcing for a fixed subcritical Reynolds number and supercritical Rayleigh number are presented. Then, several cases with fixed deterministic inflow forcing are compared with the results from the DNS with random inflow forcing. Afterward, two cases with spiral RBP basic flow with random inflow forcing are discussed. This paper concludes with a brief discussion of the results.

II. METHODOLOGY

A. Governing equations

The compressible Navier-Stokes equations in cylindrical coordinates were solved numerically. The governing equations were nondimensionalized with the channel half height, L_{ref}, inflow velocity, u_{ref}, density, ρ_{ref}, and temperature, $T_{ref} = 300\,\mathrm{K}$. The pressure, p, was made dimensionless with $\rho_{ref} u_{ref}^2$. The reference Mach number was

$M = 0.05$, and the Prandtl number was set to 1. For the chosen reference Mach number, the local Mach number remains below 0.3 everywhere in the computational domain such that the flow can be considered to be nearly incompressible. The compressible Navier-Stokes equations in cylindrical coordinates[24] can be written in vector form

$$\frac{\partial \mathbf{Q}}{\partial t} + \frac{\partial \mathbf{A}}{\partial z} + \frac{\partial \mathbf{B}}{\partial r} + \frac{1}{r}\frac{\partial \mathbf{C}}{\partial \theta} + \frac{1}{r}\mathbf{D} = \mathbf{H}, \tag{3}$$

with state vector

$$\mathbf{Q} = \left[\rho, \rho u, \rho v, \rho w, \rho e\right]^T, \tag{4}$$

and flux vectors

$$\mathbf{E}^{(i)} = \begin{bmatrix} \rho u_i \\ \rho u u_i + p\delta_{1i} - \tau_{1i} \\ \rho v u_i + p\delta_{2i} - \tau_{2i} \\ \rho w u_i + p\delta_{3i} - \tau_{3i} \\ u_i(\rho e + p) - u_j\tau_{ij} + q_i \end{bmatrix}. \tag{5}$$

Here, the Einstein notation is used where repeated indices imply a summation. The fluxes $\mathbf{E}^{(i)}$ corresponding to $i = 1, 2, 3$ are $\mathbf{E}^{(1)} = \mathbf{A}$, $\mathbf{E}^{(2)} = \mathbf{B}$, and $\mathbf{E}^{(3)} = \mathbf{C}$. The source term vectors are

$$\mathbf{D} = \begin{bmatrix} \rho v \\ \rho u v - \tau_{rz} \\ \rho v^2 - \rho w^2 - \tau_{rr} + \tau_{\theta\theta} \\ 2\rho v w - 2\tau_{\theta r} \\ v(\rho e + p) - u\tau_{rz} - v\tau_{rr} - w\tau_{\theta r} + q_r \end{bmatrix}, \tag{6}$$

and

$$\mathbf{H} = \begin{bmatrix} 0 \\ g(\rho_{ref} - \rho) \\ 0 \\ 0 \\ ug(\rho_{ref} - \rho) \end{bmatrix}. \tag{7}$$

Here, u, v, and w are the velocities in the z (wall-normal), r (streamwise), and θ (azimuthal) directions that correspond to $i = 1, 2, 3$. Subscripts indicate partial derivatives. The total energy, $e = \varepsilon + 1/2 u_i u_i$, is the sum of the internal energy, $\varepsilon = c_v T$, and the kinetic energy, where c_v is the specific heat at constant volume and T is the temperature. Vector $\mathbf{H}$ includes a buoyancy term that makes recourse to the Boussinesq approximation, $g(\rho_{ref} - \rho)$, with gravitational acceleration $g = 9.81 m/s^2$. For the present numerical analyses, the assumptions made for the Boussinesq approximation (see the study by Spiegel and Veronis[25]) are satisfied. The shear stress tensor components are

$$\tau_{zz} = \frac{2\mu}{3Re}\left[2\frac{\partial u}{\partial z} - \frac{\partial v}{\partial r} - \frac{1}{r}\left(\frac{\partial w}{\partial \theta} + v\right)\right], \tag{8}$$

$$\tau_{rr} = \frac{2\mu}{3Re}\left[-\frac{\partial u}{\partial z} + 2\frac{\partial v}{\partial r} - \frac{1}{r}\left(\frac{\partial w}{\partial \theta} + v\right)\right], \tag{9}$$

$$\tau_{\theta\theta} = \frac{2\mu}{3Re}\left[-\frac{\partial u}{\partial z} - \frac{\partial v}{\partial r} + 2\frac{1}{r}\left(\frac{\partial w}{\partial \theta} + v\right)\right], \tag{10}$$

and

$$\tau_{rz} = \frac{\mu}{Re}\left[\frac{\partial u}{\partial r} + \frac{\partial v}{\partial z}\right], \tag{11}$$

$$\tau_{\theta z} = \frac{\mu}{Re}\left[\frac{\partial w}{\partial z} + \frac{1}{r}\frac{\partial u}{\partial \theta}\right], \tag{12}$$

$$\tau_{\theta r} = \frac{\mu}{Re}\left[\frac{1}{r}\left(\frac{\partial v}{\partial \theta} - w\right) + \frac{\partial w}{\partial r}\right], \tag{13}$$

with μ being dynamic viscosity. The heat flux vector components are

$$q_z = -k\frac{\partial T}{\partial z}, \tag{14}$$

$$q_r = -k\frac{\partial T}{\partial r}, \tag{15}$$

$$q_\theta = -k\frac{1}{r}\frac{\partial T}{\partial \theta}, \tag{16}$$

with k being the heat conduction coefficient. The set of equations is closed by the ideal gas equation,

$$p = \rho R T, \tag{17}$$

with R being the gas constant and Sutherland's law for the viscosity. For the chosen reference quantities, the Rayleigh number [as defined in Eq. (2)] can be rewritten as

$$Ra = Re^2 \frac{\Delta T}{T_{av}}\left(\frac{h}{L_{ref}}\right)^3 \left(g\frac{L_{ref}}{u_{ref}^2}\right) Pr, \tag{18}$$

where $\gamma = 1/T_{av}$, with $T_{av} = (T_b + T_t)/2$ being the thermal expansion coefficient for a perfect gas, $\Delta T = T_b - T_t$ is the temperature difference between the bottom and top wall, and gL_{ref}/u_{ref}^2 is the dimensionless gravitational acceleration. The dimensionless specific heats and gas constant are $c_p = 1/[(\gamma - 1)M^2]$, $c_v = 1/[\gamma(\gamma - 1)M^2]$, and $R = c_p - c_v = 1/(\gamma M^2)$. The dimensionless heat conduction coefficient is $k = \mu/[Pr(\gamma - 1)M^2 Re]$.

B. Computational domain and discretization

A computational domain with a grid opening angle of $\Theta = 90°$ was employed for all simulations [Fig. 1(a)] except for one full domain simulation ($\Theta = 360°$). The inflow radius was $r_2 = 22.918$, and the outflow radius was $r_1 = 3$. Both r_1 and r_2 were non-dimensionalized by L_{ref}. The ratio $r_2/r_1 \approx 7.6$ was chosen such that an appreciable streamwise flow acceleration was obtained. The choice of the distance $r_2 - r_1 \approx 20$ was based on two considerations: (1) to provide a sufficient streamwise domain extent to allow the disturbance amplitudes to grow several orders of magnitude and (2) to limit the computational expense of the simulations. A wall-normal coordinate transformation was employed, and grid points were clustered near the walls[12] based on the analytical relationship,

$$z_j = \left[\frac{\tan^{-1}(jc - f_1)}{f_2} + 1\right] \times \frac{h}{2}, \tag{19}$$

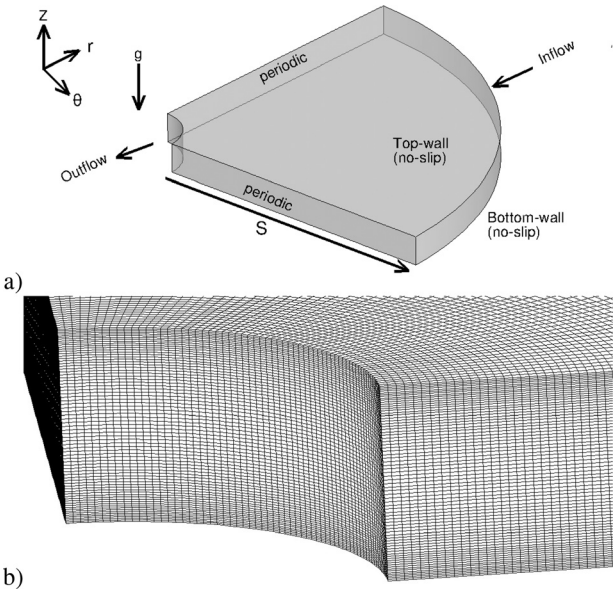

FIG. 1. (a) Computational domain for $\Theta = 90°$ simulation and (b) detail of the grid near outflow boundary.

where $h = 2$ is the channel height, $f_1 = c^* jx/2$, $f_2 = \tan^{-1}(f_1)$, $c^* = 0.05$ is a user-specified constant, j is the grid line index, and jx is the total number of grid points in the wall-normal direction. An equidistant grid point distribution was employed in the streamwise direction. The details of the computational grid with $ix = 240$, $jx = 72$, and $kx = 64$ are given in Fig. 1(b).

The spatial DNS code is an extension of an in-house developed temporal DNS code based on Cartesian coordinates, which was successfully employed for investigating the primary and secondary instability of plane RBP flow.[12,13] The convective terms in the wall-normal and radial direction are discretized with fifth-order accurate upwind-biased and downwind-biased compact finite differences.[26] The first and second derivatives of the viscous terms (wall-normal and radial direction) are discretized with fourth-order accurate compact finite differences for non-equidistant meshes by Shukla *et al.*[27] Derivatives in the periodic azimuthal (θ-coordinate) direction are calculated in spectral space using forward and backward fast Fourier transforms. A fourth-order accurate explicit low-storage Runge-Kutta method[28] is employed for time integration. The number of grid points in the streamwise and wall-normal direction, ix and jx, as well as the number of azimuthal Fourier modes, kx, for the different cases discussed in this paper are summarized in Table I.

C. Boundary conditions

No-slip and no-penetration boundary conditions were imposed at both the top and bottom walls. The temperature of the bottom wall, $T_b = 350$ K, and top wall, $T_t = 300$ K, were held constant. The values of T_b and T_t were the same as in the previous work by the authors.[12,13] The bottom and top wall pressure were obtained from one-sided finite difference stencils as explained in the study by Hasan and Gross.[12] The spectral discretization in the azimuthal direction implicitly enforces flow periodicity. At the inflow boundary, a nonreflecting boundary condition based on Riemann invariants[29] was applied. A characteristic-based boundary condition[30] was employed at the outflow boundary. The reference profiles required by both boundary conditions were generated by solving the one-dimensional Navier-Stokes equations for laminar plane RBP flow,

$$\frac{\partial p}{\partial x} = \mu \frac{\partial^2 u^*}{\partial y^2}, \tag{20}$$

$$\frac{\partial p}{\partial y} = (1 - \rho) g, \tag{21}$$

$$k \frac{\partial^2 T}{\partial y^2} + \mu \left(\frac{\partial u^*}{\partial y} \right)^2 = 0. \tag{22}$$

Here, x, y, and u^* refer to the streamwise coordinate, wall-normal coordinate, and streamwise velocity in the Cartesian system.

TABLE I. Streamwise and wall-normal number of grid points and number of azimuthal Fourier modes.

Grid	Re[a]	Ra	Resolution
a	200	500 000	$ix = 120$, $jx = 48$, $kx = 32$
b	200	500 000	$ix = 240$, $jx = 48$, $kx = 32$
c	200	500 000	$ix = 360$, $jx = 48$, $kx = 32$
d	200	500 000	$ix = 240$, $jx = 72$, $kx = 32$
e	200	500 000	$ix = 240$, $jx = 120$, $kx = 32$

[a]Reference inflow Reynolds number.

D. Numerical linear stability analysis

Both straight (purely radial) and spiral basic flows were considered. The nominal inflow angles as defined by $\tan^{-1}(|w|/|v|)$ for the spiral flow cases were 22.5 and 45°. In the experiments, inflow guide vanes could be employed to deflect the flow in the azimuthal direction and create a swirl. The different cases that were investigated fall into two categories: a) "uncontrolled" cases and (b) "controlled" cases. For the uncontrolled cases, unsteady randomized (based on the FORTRAN subroutine "random_number") velocity disturbances with a maximum amplitude of 10^{-6} were added to the basic flow at the inflow boundary to excite a broad spectrum of frequencies and a wide range of streamwise and azimuthal wavenumbers. The maximum amplitude of the velocity disturbances was such that the disturbance amplitudes remained linear throughout the domain. For the controlled cases, mode shapes from precursor simulations were introduced at the inflow boundary to force one specific mode. The different cases are tabulated in Table II. For both categories, the simulation data obtained from the DNS were Fourier transformed in time and then Fourier transformed in the azimuthal direction. From these double Fourier transformed data, the growth rates, wave angles, and phase speeds of the disturbance waves were computed.

Similar to linear stability theory (LST), a wave ansatz of the form

$$u'(r, z, \theta, t) = \sum \hat{u}(z) e^{i(\alpha r + \beta\theta - \omega t)} \tag{23}$$

is made for the disturbances. Here, $\alpha = \alpha_r + i\alpha_i$ and β are the radial and azimuthal wavenumbers, respectively, and $\omega = \omega_r + i\omega_i$ is the angular frequency. The mode shapes (eigenfunctions in linear stability theory)

TABLE II. Parameters for investigated cases.

Case	Re[a]	Ra	Type of flow
1	200	500 000	Radial (0°); random forcing
2	200	500 000	Radial; controlled forcing ($\omega = 0.245$)
3	200	500 000	Radial; controlled forcing ($\omega = 1.472$)
4	200	500 000	Radial; controlled forcing ($\omega = 2.945$)
5	200	500 000	Radial (360°); random forcing
6	200	500 000	Spiral (22.5°); random forcing
7	200	500 000	Spiral (45°); random forcing

[a]Reference inflow Reynolds number.

are defined by $\hat{u}(z)$. Since the disturbances grow in space for the present spatial simulations, the temporal growth rates, ω_i, are zero and the spatial growth rates, α_i, are negative for growing waves. The radial wavenumber, $\alpha_r = 2\pi/\lambda_r$, and azimuthal wavenumber, $\beta = 2\pi/\lambda_\theta$, are linked to the radial wavelength, λ_r, and the azimuthal wavelength, λ_θ. The real part of the angular frequency, ω_r, and period, T, are connected through $\omega_r = 2\pi/T$. The temporal and azimuthal mode numbers are denoted by n and k, respectively.

The wall-normal disturbance velocity at a particular location can be described by

$$u'(r,z,\theta,t) = \hat{a}_{cc}(r,z)\cos\omega t\cos\beta r\theta + \hat{a}_{cs}(r,z)\cos\omega t\sin\beta r\theta + \hat{a}_{sc}(r,z)\sin\omega t\cos\beta r\theta + \hat{a}_{ss}(r,z)\sin\omega t\sin\beta r\theta. \tag{24}$$

Here, the spanwise wavenumber and frequency are $\beta = 2\pi k/(r\Theta)$ and $\omega_r = 2\pi n/T$, respectively. The first subscript refers to the time (cosine and sine mode), and the second subscript refers to the azimuthal direction. The coefficients are used to obtain the amplitude and phase of the right traveling waves (in the positive θ-direction, "+" superscript),

$$A = \sqrt{(\hat{a}_c^+)^2 + (\hat{a}_s^+)^2} \tag{25}$$

and

$$\psi = -\tan^{-1}\frac{\hat{a}_s^+}{\hat{a}_c^+}, \tag{26}$$

where $\hat{a}_c^+ = (\hat{a}_{cc} + \hat{a}_{ss})/2$ and $\hat{a}_s^+ = (\hat{a}_{cs} - \hat{a}_{sc})/2$. Similarly, the amplitude and phase of the left traveling waves (in negative θ-direction, "-" superscript) are

$$A = \sqrt{(\hat{a}_c^-)^2 + (\hat{a}_s^-)^2} \tag{27}$$

and

$$\psi = -\tan^{-1}\frac{\hat{a}_s^-}{\hat{a}_c^-}, \tag{28}$$

with $\hat{a}_c^- = (\hat{a}_{cc} - \hat{a}_{ss})/2$ and $\hat{a}_s^- = -(\hat{a}_{cs} + \hat{a}_{sc})/2$. The spatial growth rates can be computed from the amplitude via

$$\alpha_i = -\frac{\partial \ln A}{\partial s}, \tag{29}$$

where $s = (r_2 - r)$ is the streamwise coordinate measured from the inflow and r is the local radius. The phase is defined as $\psi = \alpha_r r + \beta r\theta - \omega_r t$. The phase speed in the radial direction is

$$c_r = -\frac{\frac{\partial\psi}{\partial t}}{\frac{\partial\psi}{\partial r}} = \frac{\omega_r}{\alpha_r}, \tag{30}$$

and the phase speed in the wave propagation direction is

$$c = \frac{\omega_r}{K}, \tag{31}$$

where $K = \sqrt{\alpha_r^2 + \beta^2}$. The wave angle is obtained from

$$\phi = \tan^{-1}\frac{\beta}{\alpha_r}. \tag{32}$$

III. BASIC FLOWS

Direct numerical simulations without any inflow forcing were carried out first to obtain the basic flows. The basic flow simulations were advanced in time until all disturbance amplitudes decayed to machine zero. Simulations with random and controlled inflow forcing were then carried out, and detailed analyses of the flow were performed for three streamwise locations, $s = 9.96$, 12.45, and 14.94. A schematic indicating the three streamwise locations is shown in Fig. 2. In this figure, $s = 0$ indicates the inflow and $s = 19.918$ is the outflow.

The radial and azimuthal velocity profiles obtained from the basic flow simulations for the case with radial and swept (spiral) inflow are plotted in Fig. 3. It can be noticed that the radial velocity increases almost hyperbolically (it becomes more negative for the chosen coordinate system) in the radial direction and approximately follows a $\rho v \propto 1/r$ relationship due to the conservation of mass. The azimuthal velocity for the simulation with radial inflow is zero. However, for the spiral flow cases, the azimuthal velocity increases in the streamwise direction. As the flow accelerates, both the pressure gradient and temperature decrease (Fig. 4). Included in the top image of Fig. 4 is the analytical pressure gradient for laminar plane channel flow, $2/Re$. This value is approached asymptotically near the inflow by the radial basic flow.

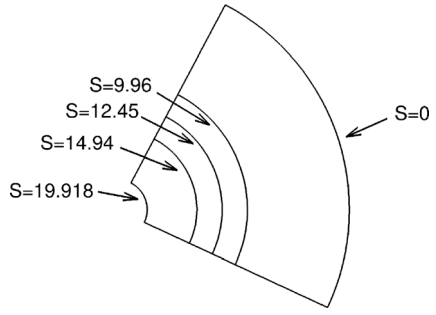

FIG. 2. Schematic showing streamwise locations for detailed analyses.

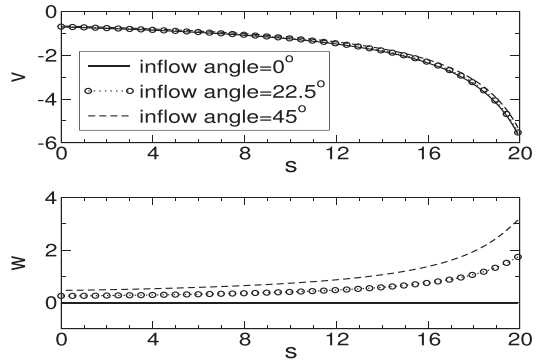

FIG. 3. Channel half-height radial and azimuthal velocity for basic flows. Here and in the following figures, $s = r_2 - r$. The velocities were made dimensionless with u_{ref}.

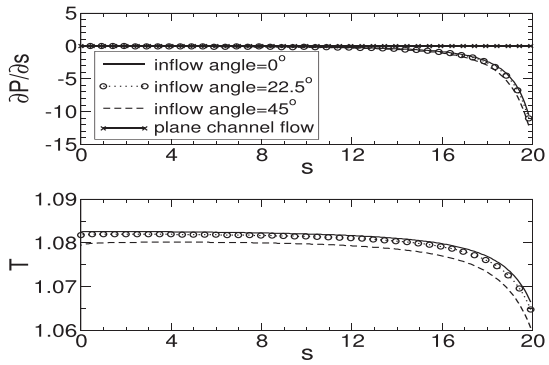

FIG. 4. Channel half-height pressure and temperature for basic flows. Pressure and temperature were made dimensionless with $\rho_{ref} u_{ref}^2$ and $T_{ref} = 300$ K, respectively.

Figure 5 (top) presents radial velocity profiles plotted vs the channel height for three radial locations, which are $s = 3.319\,(r = 19.599)$, $s = 9.959\,(r = 12.959)$, and $s = 17.429\,(r = 5.489)$. For the basic flow simulation with radial inflow, closer to the outflow (s = 17.429), the radial velocity profile is much fuller and more asymmetric compared to the location closer to the inflow (s = 3.319). For the simulations with swept inflow, the radial velocity profiles lose their

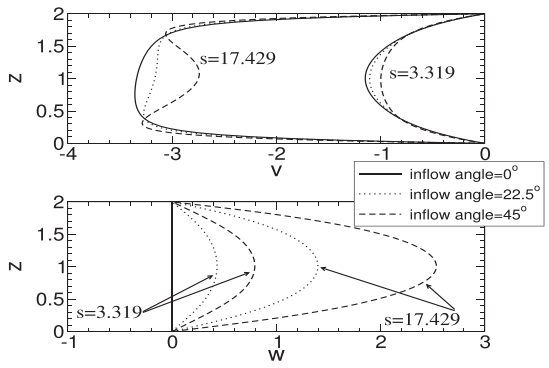

FIG. 5. Basic flow profiles of radial and azimuthal velocity.

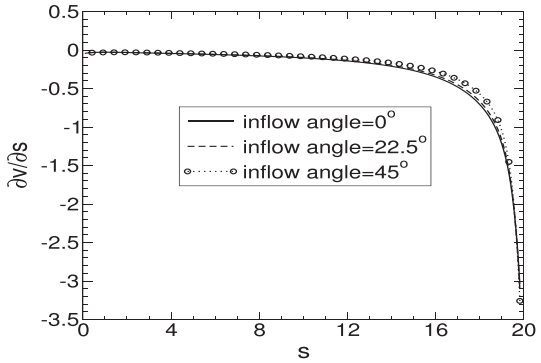

FIG. 6. Basic flow radial acceleration at the channel half height.

almost parabolic character close to the outflow. Figure 5 (bottom) shows the azimuthal velocity profiles for the same three radial locations. Unlike the radial velocity profiles, the azimuthal velocity profiles appear symmetric and parabolic for all basic flow simulations (swept and unswept). Figure 6 illustrates a strongly increasing streamwise acceleration, $\partial v/\partial s$, toward the outflow boundary. Streamwise acceleration has a stabilizing effect on boundary layer flows.[14] Therefore, based on Fig. 6, a noticeable stabilization of the flow is expected near the outflow.

IV. RESULTS

A. Radial RBP flow

1. Uncontrolled cases

The reference Reynolds number and Rayleigh number for the first simulation (case 1) are $Re = 200$ and $Ra = 500\,000$. The Rayleigh number and local Reynolds number (which increases due to the radial acceleration) for the present simulation together with the neutral curves for plane RBP flow by Gage and Reid[1] are shown in Fig. 7. According to Gage and Reid[1] for $Re < Re_c = 5400$ and $Ra > Ra_c = 1708$, the flow is unstable with respect to buoyancy-driven instability and 3-D waves with a wave angle of 90° are most amplified. On the contrary, for $Re > Re_c = 5400$ and $Ra < Ra_c = 1708$, viscosity-driven instability occurs and 2D Tollmien–Schlichting waves are most unstable. The stability boundaries also indicate that as the Rayleigh number increases

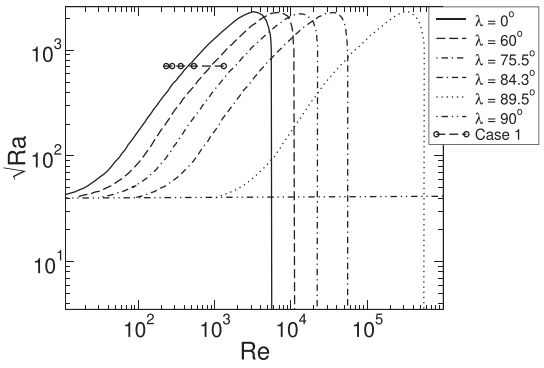

FIG. 7. Conditions for case 1 and neutral curves in the study by Gage and Reid.[1]

for a fixed $Re < Re_c$, oblique waves with a progressively smaller wave angle become amplified. According to Gage and Reid,[1] case 1 should exhibit buoyancy-driven instability. Several spatial DNSs with random forcing were carried out for three different streamwise grid resolutions ($ix = 120$, 240, and 360, with ix being the number of grid points in the streamwise direction) to investigate grid convergence. The number of points in the wall-normal direction, $jx = 48$, and the number of azimuthal modes, $kx = 32$, were held constant (grids a, b, and c in Table I). Figure 8 shows spatial growth rate contours for different frequencies and azimuthal wavenumbers at $s = 12.45$ (closer to the outflow). The temporal linear stability analysis by Gage and Reid[1] predicts

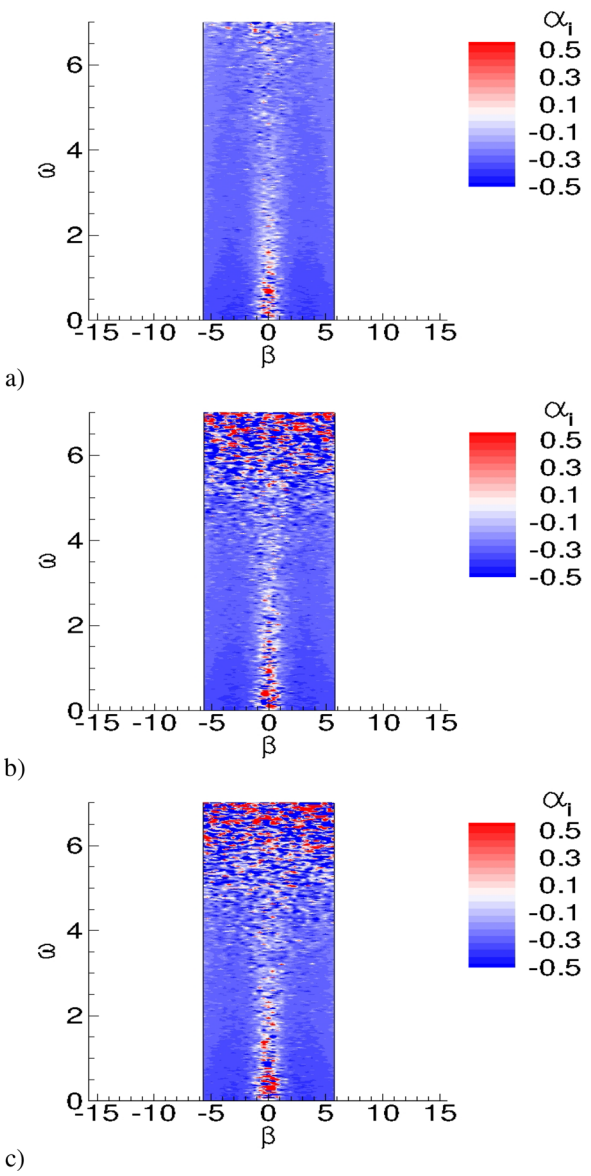

FIG. 8. Contours of spatial growth rate at $s = 12.45$ for (a) $ix = 120$, (b) $ix = 240$, and (c) $ix = 360$ for case 1. α_i and β are non-dimensionalized with $1/L_{ref}$, and ω is non-dimensionalized with u_{ref}/L_{ref}.

that for the chosen conditions, oblique waves are amplified. Interestingly, Figs. 8(a)–8(c) also show amplified oblique waves for the inward radial RBP flow. The positive β values correspond to right-traveling waves, while the negative β values correspond to left-traveling waves. A qualitative comparison of the growth rates for the different streamwise grid resolutions in Fig. 8 reveals no significant differences. A quantitative comparison of the amplitudes for steady azimuthal mode $k = 9$ and growth rates for $\beta = 3.43$ is provided in Fig. 9. In Fig. 9 (bottom), the gray lines are raw data and the black lines are for data that were filtered over a frequency interval of $\Delta\omega = 0.38$ according to

$$\hat{\alpha}_i(\omega) = \frac{1}{\Delta\omega}\int_{\omega-\frac{\Delta\omega}{2}}^{\omega+\frac{\Delta\omega}{2}} \alpha_i(\omega')d(\omega'), \tag{33}$$

where $\hat{\alpha}_i(\omega)$ is the filtered data. As the number of streamwise grid points is increased, the amplitudes (Fig. 9, top image) and the growth rates (Fig. 9, bottom image) converge. Based on this grid convergence study, it was decided to use $ix = 240$ grid points in the streamwise direction. Next, a wall-normal grid convergence study was conducted. The spatial growth rate contours at $s = 12.45$ for three different wall-normal grid resolutions ($jx = 48$, 72, and, 120) (grids b, d, and e in Table II), fixed $ix = 240$ and 32 azimuthal modes are plotted in Fig. 10. A quantitative comparison of the amplitudes for steady azimuthal mode $k = 9$ and growth rate distributions for $\beta = 3.43$ is shown in Fig. 11(top) and Fig. 11 (bottom), respectively. Grid convergence is observed for $jx = 72$. Based on these results, the wall-normal number of grid points was set to 72.

After deciding on the grid resolution, a DNS for case 1 was carried out with $ix = 240$, $jx = 72$, and 64 azimuthal modes. The same resolution was employed for all following cases. Contours of the azimuthal velocity at the channel mid-height in Fig. 12 exhibit steady azimuthal 3D waves. Figure 12 also shows an apparent "merging" of waves (indicated by circles) in the downstream direction. This

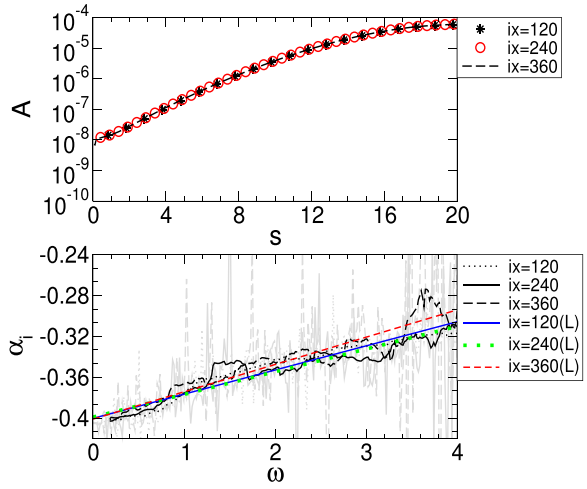

FIG. 9. Amplitudes for steady azimuthal mode $k = 9$ vs streamwise coordinate (top) and growth rates vs frequency at $s = 12.45$ (bottom) for different numbers of streamwise grid points (L = linear regression). In the bottom figure, gray lines represent raw data and black lines are for data filtered over a frequency interval of $\Delta\omega = 0.38$.

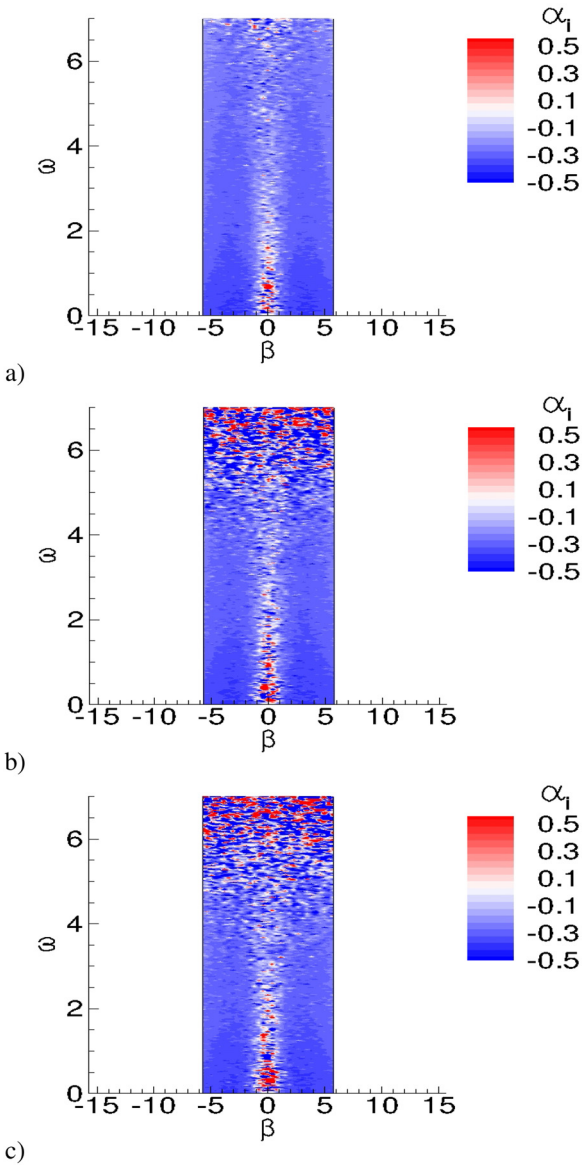

FIG. 10. Contours of the growth rate at $s = 12.45$ for (a) $jx = 48$, (b) 72, and (c) 120 for case 1.

phenomenon occurs because for a specific radial location, the azimuthal wavelength has to be an integer fraction of the circumference, $2\pi r/k$. This prevents a gradual smooth transition of the wavelength as the channel gets narrower. If the wave amplitudes were to reach nonlinear levels, this could affect possible secondary instabilities. Contours of the growth rate for different frequencies and azimuthal wavenumbers and three different streamwise locations ($s = 9.96$, 12.45, and 14.94) are plotted in Fig. 13. The location $s = 9.96$ is at the radial halfway point and $s = 14.94$ is closer to the outflow (Fig. 2). For $\omega > 8$, the disturbance amplitudes are very small, which introduces a lot of noise when computing the spatial growth rates. Figures 13(a)–13(c) illustrate that the spatial growth rates decrease in the downstream

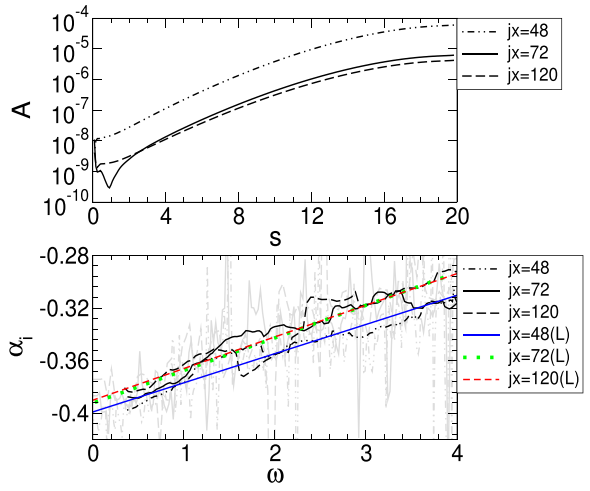

FIG. 11. Amplitudes for steady azimuthal mode $k = 9$ vs streamwise coordinate (top) and growth rates vs frequency at $s = 12.45$ (bottom) for different numbers of wall-normal grid points (L = linear regression). In the bottom figure, gray lines represent raw data and black lines are for data filtered over a frequency interval of $\Delta\omega = 0.76$.

direction. This confirms that the strong streamwise acceleration stabilizes the inward radial RBP flow. This finding is in agreement with stability analyses for boundary layer flows.[14] Figures 13(a)–13(c) also show that steady waves ($\omega = 0$) have the highest growth rates. The growth rates of the left- and right-traveling oblique waves are almost identical and decrease with frequency. Steady waves with an azimuthal wavenumber of $\beta \approx 3.43$ exhibit the largest growth rates for all three radial locations. The corresponding wavelength is 1.83 and, thus, slightly less than the channel height. In Fig. 14, the amplitudes and growth rates of the steady modes computed from the wall-normal disturbance velocity at the channel mid-height are plotted vs the streamwise coordinate. The disturbances are linear, which is confirmed by the amplitude distributions [Fig. 14(a)]. Interestingly, lower and lower azimuthal wavenumbers are amplified as the flow travels downstream. Mode $k = 10$ is most amplified near the inflow, while mode $k = 1$ has the highest growth rate near the outflow [Fig. 14(b)]. Because only integer multiples of the azimuthal wavelength are possible, this transition to lower azimuthal mode numbers is discrete and leads to the apparent merging of waves in Fig. 12 as discussed earlier.

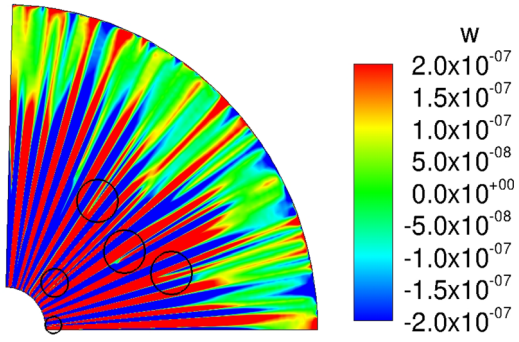

FIG. 12. Azimuthal velocity contours at the mid-channel height.

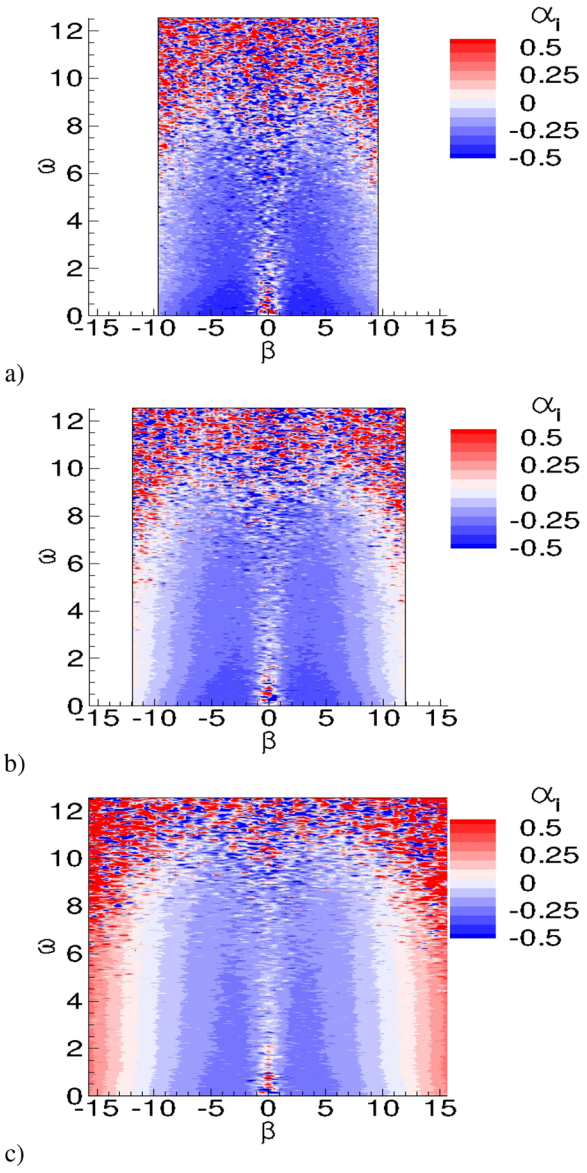

FIG. 13. Contours of the growth rate for (a) $s = 9.96$, (b) $s = 12.45$, and (c) $s = 14.94$ for case 1.

The contours in Fig. 15(a) for $s = 12.45$ demonstrate how the phase speed acts with frequency and azimuthal wavenumber. It is observed that the phase speed of the steady azimuthal waves is zero. The phase speed of both the left- and right-traveling waves becomes larger with increasing frequency. For a fixed frequency, the phase speeds of both families of oblique waves decrease with the increasing azimuthal wavenumber. The wave angle gets smaller with increasing frequency and larger with the increasing azimuthal wavenumber [Fig. 15(b)]. These results are in agreement with the plane channel flow analyses by Hasan and Gross,[12] which also revealed that the amplification increases with the wave angle and decreases with phase speed. As

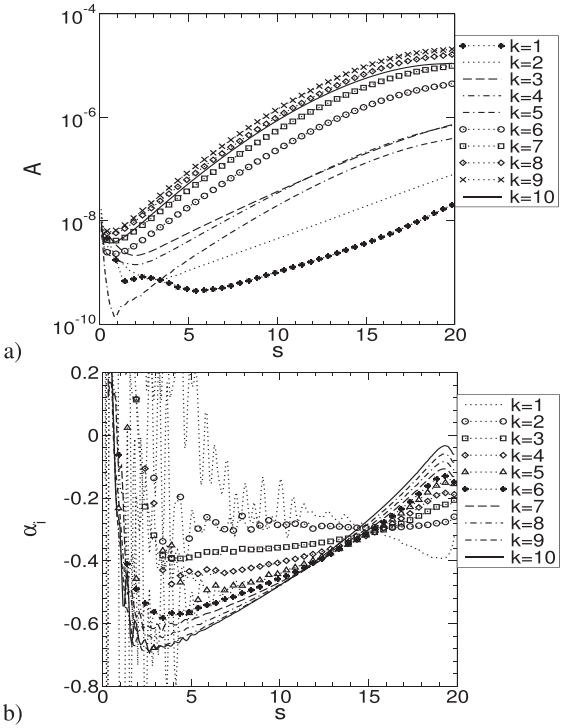

FIG. 14. (a) Amplitude and (b) growth rate of steady waves vs streamwise coordinate for case 1.

mentioned previously, the radial acceleration, $\partial v/\partial s$, increases almost hyperbolically in the streamwise direction (Fig. 6). Figure 16 shows that the growth rates of the steady waves get lower as the radial acceleration increases. Figure 16 also confirms that higher azimuthal mode numbers are more amplified near the inflow and lower azimuthal mode numbers are more amplified near the outflow.

Figures 17(a)–17(c) show the $k = 9$ disturbance amplitudes at the channel mid-height for the steady waves, $\omega = 0$, and for the left- and right-traveling oblique waves with $\omega = 1.227$. The wave fronts of the steady waves are aligned in the radial direction [Fig. 17(a)]. The wave fronts of the right- [Fig. 17(b)] and left-traveling oblique waves [Fig. 17(c)] are at an angle to the radial direction and symmetric with respect to each other. It is also noticed that the wave angle of the left- and right-traveling waves increases in the streamwise direction. This behavior is in agreement with the study by Gage and Reid[1] who found that as the Reynolds number increases for a fixed unstable Rayleigh number, $Ra > Ra_c = 1708$, the wave angle of the unstable oblique waves increases (Fig. 7). The growth rates for the steady waves are overall higher than for the oblique waves. As a result, the steady waves reach higher disturbance amplitudes as seen in Fig. 17(d).

2. Controlled cases

Several DNSs with controlled inflow forcing (case 2–case 4) were carried out for the same simulation parameters as for case 1. Toward that end, disturbance amplitude distributions for specific frequencies and azimuthal mode numbers were extracted from the case 1 DNS

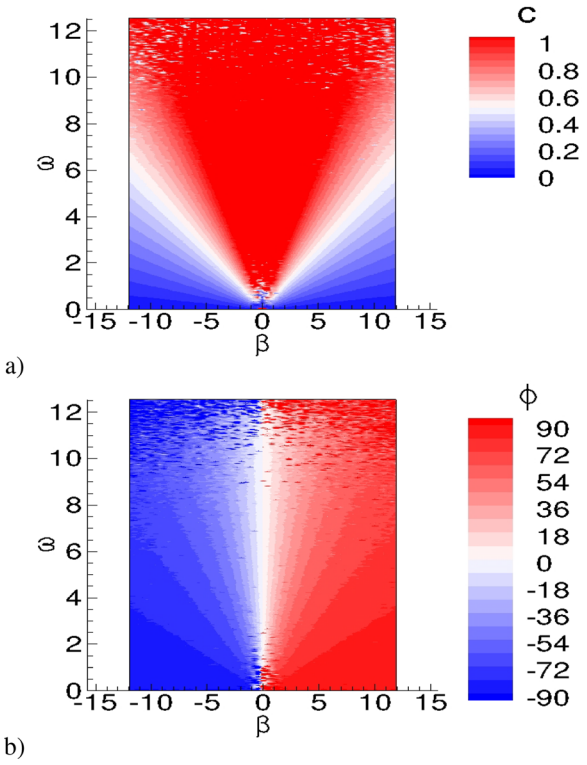

FIG. 15. Contours of (a) phase speed and (b) wave angle for $s = 12.45$ for case 1. The phase speed is made dimensionless with u_{ref}.

and introduced at the inflow boundary to excite waves with specific frequencies ($\omega = 0.245$ for case 2, $\omega = 1.472$ for case 3, and $\omega = 2.945$ for case 4) and one fixed azimuthal mode number, $k = 9$. Mode $k = 9$ corresponds to the azimuthal wavenumber, $\beta = 3.43$ at $s = 12.45$. The modes were scaled such that the maximum wall-normal disturbance velocity amplitude was 7×10^{-9}. The objective was to confirm the growth rates, phase speeds, and wave angles obtained from the simulation with random forcing. In Fig. 18 (top), distributions of the spatial growth rate are plotted over the streamwise coordinate. The growth rates decrease with increasing frequency and

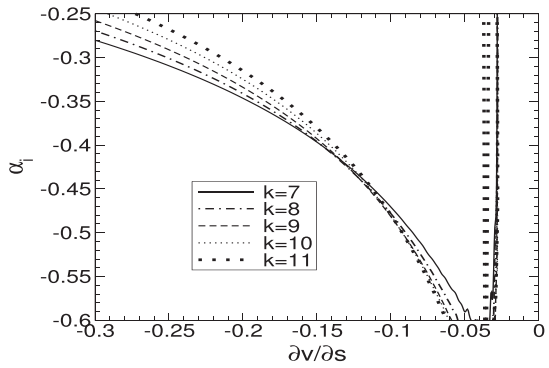

FIG. 16. Growth rates for steady waves vs radial acceleration for case 1.

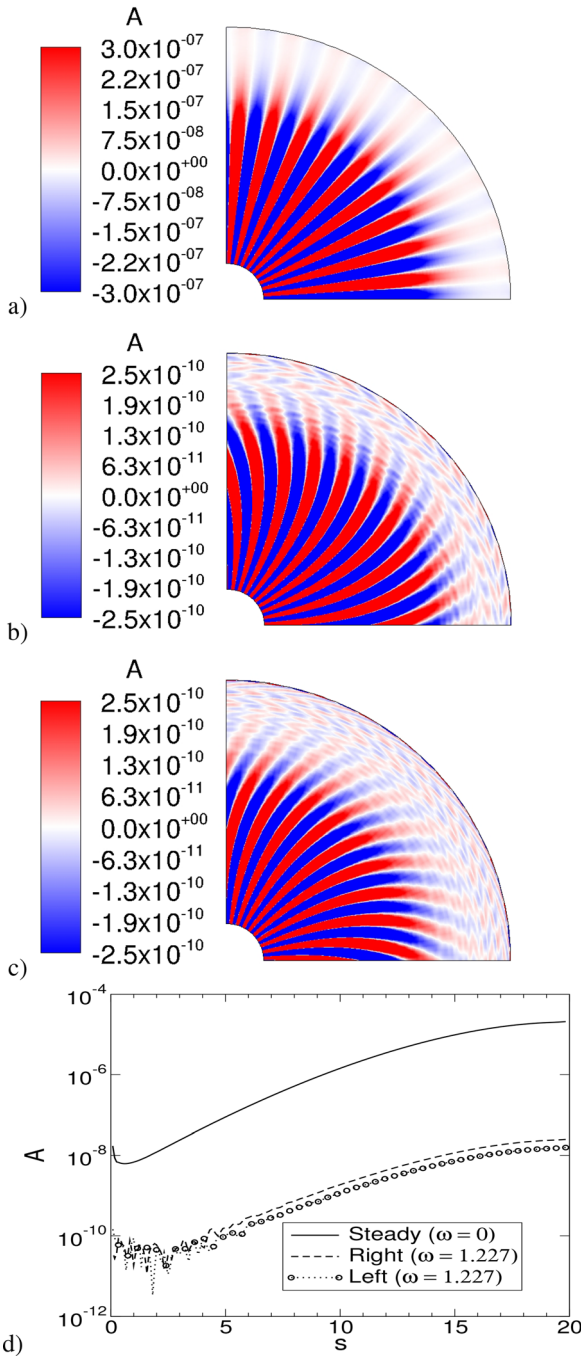

FIG. 17. Iso-contours of wall-normal disturbance velocity amplitude at the channel mid-height for $k = 9$ (case 1): (a) steady waves ($\omega = 0$), (b) right traveling waves ($\omega = 1.227$), and (c) left traveling waves ($\omega = 1.227$). d) Mode amplitudes vs streamwise coordinate for $k = 9$.

streamwise acceleration. The growth rates of the left- and right-traveling waves are identical. In Fig. 18 (bottom), the growth rates for $\beta = 3.43$ at $s = 12.45$ obtained from the simulation with random forcing [data were extracted from Fig. 13(b)] are compared with the

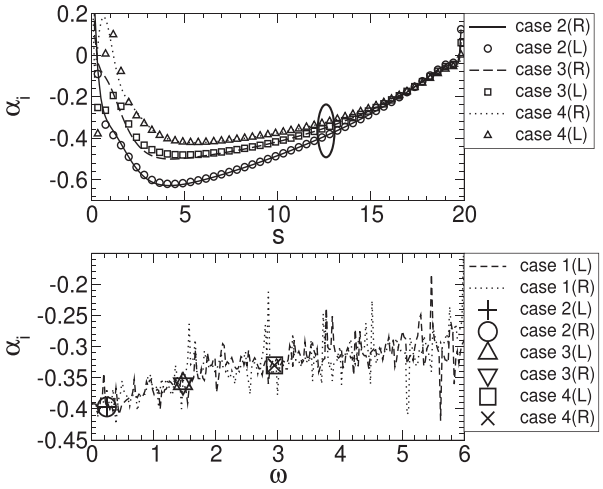

FIG. 18. Spatial growth rate vs streamwise coordinate (controlled forcing) (top) and frequency (bottom) at $s = 12.45$ (random forcing: case 1). L and R represent left- and right-traveling waves.

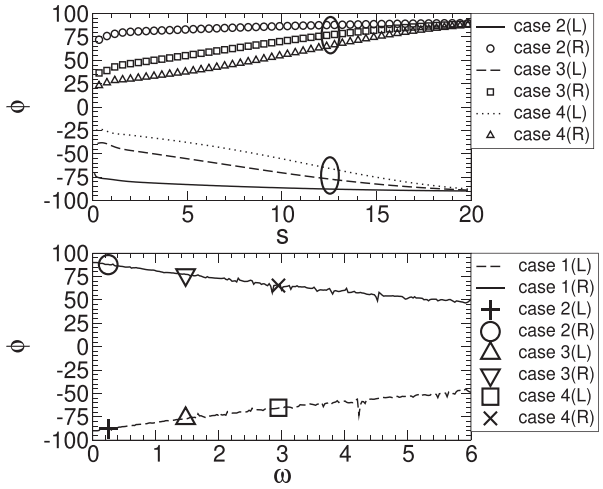

FIG. 20. Wave angle vs (a) streamwise coordinate (controlled forcing) and (b) frequency at $s = 12.45$ (random forcing: case 1). L and R represent the left- and right-traveling waves.

growth rates at $s = 12.45$ obtained from the simulations with controlled forcing (symbols). The growth rates obtained from the former are in good agreement with the growth rates obtained from the latter. This validates the random forcing approach, which provides the stability characteristics for a wide frequency and wavenumber range based on a single simulation. This makes it computationally more efficient than running separate simulations for each individual frequency and azimuthal wavenumber.

In Fig. 19 (top), the phase speeds obtained from the simulations with controlled forcing are graphed vs the streamwise coordinate. The phase speeds decrease in the streamwise direction and increase with frequency. The phase speeds of both oblique waves are very close. For $s = 12.45$, the phase speed for $\beta = 3.43$ from the simulation with random forcing [Fig. 15(a)] is in close agreement with the phase speed from the simulations with controlled forcing (lines and symbols in Fig. 19, bottom). Unlike the phase speeds, the wave angles for both the left- and right-traveling waves obtained from the simulations with controlled forcing (case 2–case 4) increase in the streamwise direction and decrease with frequency as seen in Fig. 20 (top). As for the growth rates and phase speeds, the wave angles from the DNS with controlled forcing match the wave angles from the DNS with random forcing very well, as can be seen in Fig. 20 (bottom). Wall-normal disturbance amplitude distributions for $s = 12.45$ are given in Fig. 21. The distributions obtained for the left- and right-traveling waves are nearly identical. The v' and w' amplitude distributions have two peaks near $z \approx 1.8$ and $z \approx 0.2$. The amplitude distributions for T' also exhibit two weak maxima. The u' disturbance amplitude distributions have only a singular peak near the mid-channel height. The fact that the amplitude distributions for cases 1 and 2 are in close agreement provides further justification for the random forcing approach.

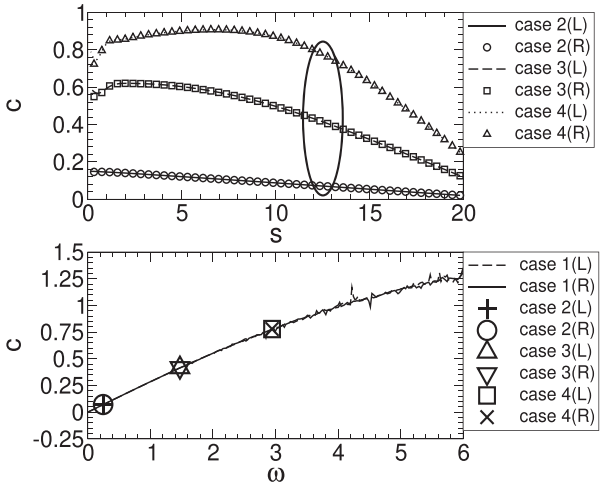

FIG. 19. Phase speed vs (a) streamwise coordinate (controlled simulations) and (b) frequency at $s = 12.45$ (uncontrolled simulation: case 1). L and R represent the left- and right-traveling waves.

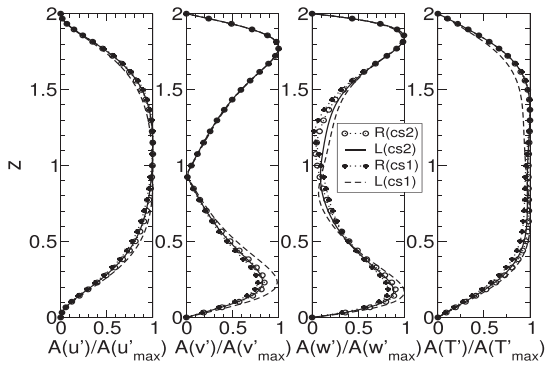

FIG. 21. Normalized disturbance amplitudes at $s = 12.45$ for $\omega = 0.245$ and $k = 9$ ($\beta = 3.43$) for cases 1 and 2.

3. Full domain simulation-360°

To confirm that the restriction to a quarter segment of the radial flow does not affect the result, and to check if the resolution of the low azimuthal wavenumbers is sufficient, a radial flow (no inflow angle) simulation with random forcing for a 360° computational domain was performed (case 5). The Reynolds and Rayleigh number and grid resolution were the same as for case 1. Since the number of azimuthal modes was the same as for case 1, the largest azimuthal wavenumber that can be resolved is four times smaller than for case 1. This choice was made on purpose to limit the computational expense.

The spatial growth rate contours at $s = 14.94$ for case 5 are very similar to those for case 1 [Figs. 13(c) and 22(a), respectively]. For both cases, the steady waves ($\omega = 0$) exhibit the largest growth rates. The most amplified steady waves for case 5 have an azimuthal wavenumber of $\beta \approx 3.4$, which is very close to the respective value for case 1. The unstable regions and growth rates of the left- and right-traveling oblique waves for cases 1 and 5 are basically identical. The growth rates for $\beta \approx 3.55$ at $s = 14.94$ obtained from cases 1 and 5 are compared in Fig. 22(b) and match well. In summary, the stability characteristics for the full domain are in close agreement with those for the 90° domain. This was expected as the disturbance amplitudes were chosen small enough for the linear superposition principle to hold.

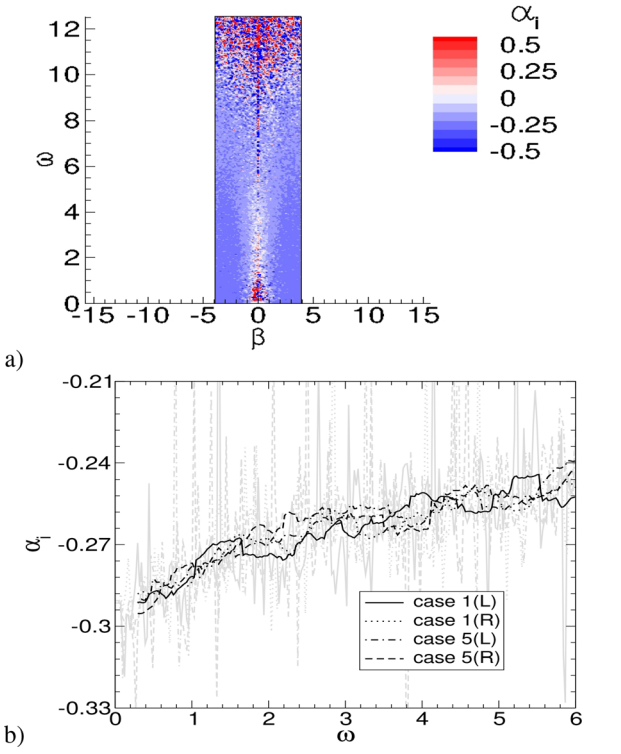

FIG. 22. (a) Contours of the growth rate for case 5 and (b) comparison of growth rates for $s = 14.94$ and $\beta \approx 3.55$ obtained from cases 1 and 5. In (b), gray lines represent raw data and black lines are for data filtered over a frequency interval of $\Delta\omega = 0.612$.

B. Spiral RBP flow-22.5°

A DNS with an inflow angle of 22.5° and random forcing (case 6) was carried out for $Re = 200$ and $Ra = 500\,000$ (the same as case 1). The dependence of the spatial growth rate on the frequency and azimuthal wavenumber for three streamwise coordinates ($s = 9.96$, 12.45, and 14.94) is exhibited in Fig. 23. Surprisingly, for the spiral basic flow, the growth rates of the left- and right-traveling oblique waves with identical azimuthal wavenumber magnitude differ. Compared to the right-traveling waves, the left-traveling waves have higher growth rates and the corresponding unstable regions in Fig. 23 are larger compared to the radial flow case. The opposite observations can be made for the

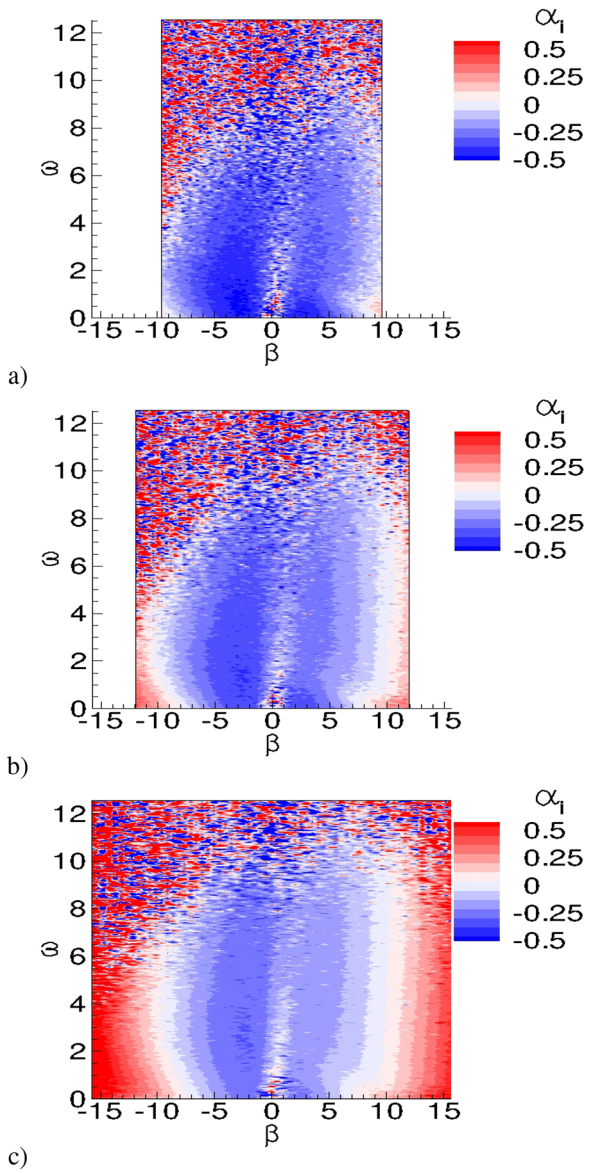

FIG. 23. Contours of the growth rate for (a) $s = 9.96$, (b) $s = 12.45$, and (c) $s = 14.94$ for case 6.

right-traveling waves. This means that one family of waves is favored over the other. Similar to the radial RBP flow, as the disturbance waves travel downstream, the growth rates overall decrease because of the streamwise acceleration. However, the azimuthal wavenumber associated with the most amplified waves is lower ($\beta \approx 2.75$) for the spiral flow than for the purely radial flow ($\beta \approx 3.43$). Also, the dependence of the growth rate on the frequency is quite different for the spiral RBP flow compared to the radial RBP flow. For instance, the growth rates for azimuthal wavenumbers in the range, $\beta \approx -5$ to $\beta \approx -8$ (left-traveling waves) in Figs. 23(a)–23(c), first increase up to $\omega \approx 2$ and then decrease as the frequency increases, while for the radial flow, the growth rates always decrease with increasing frequency.

To allow for a more detailed quantitative comparison between the stability characteristics of the radial and spiral RBP flow, the growth rates, phase speeds, and wave angles at $s = 12.45$ for a fixed azimuthal wavenumber, $\beta = 3.43$, and different frequencies are compared in Fig. 24(a). For the spiral flow case (case 6), the growth rate of the right-traveling wave is much lower than the growth rate of the left-traveling wave. In comparison, for the radial RBP flow (case 1), the growth rates of both waves are nearly identical. The growth rate of the left-traveling wave for the spiral flow first increases up to $\omega \approx 2$ and then decreases with frequency. Interestingly, for the right-traveling wave, the growth rate decreases monotonously with frequency (case 6). Figure 24(b) illustrates the dependence of the phase speed on the frequency for the radial and spiral RBP flow. While the phase speeds of the left- and right-traveling waves are identical for the radial flow case, for the spiral flow case, the right-traveling waves are faster than the left-traveling waves. For the spiral flow case, the left-traveling waves have lower wave angles than the right-traveling waves [Fig. 24(c)]. Figure 24(c) demonstrates that the wave angles of the oblique waves are symmetric with respect to $\phi = 0°$ for the radial RBP flow and $\phi \approx 9°$ (flow angle for chosen streamwise location) for the spiral RBP flow. For both cases, the wave angles decrease with frequency. Wall-normal disturbance amplitude distributions at the mid-channel height for the steady waves ($\omega = 0$) and oblique waves ($\omega = 1.227$) with $k = 9$ are shown in Fig. 25. The wave fronts for the steady waves are spiral as seen in Fig. 25(a). Different from the radial flow case, the wave fronts for the left- and right-traveling waves [Figs. 25(b) and 25(c)] are not symmetric with respect to the radius. It is also noticed that the left-traveling waves have higher amplitudes than the right-traveling waves, which can be attributed to the larger growth rates.

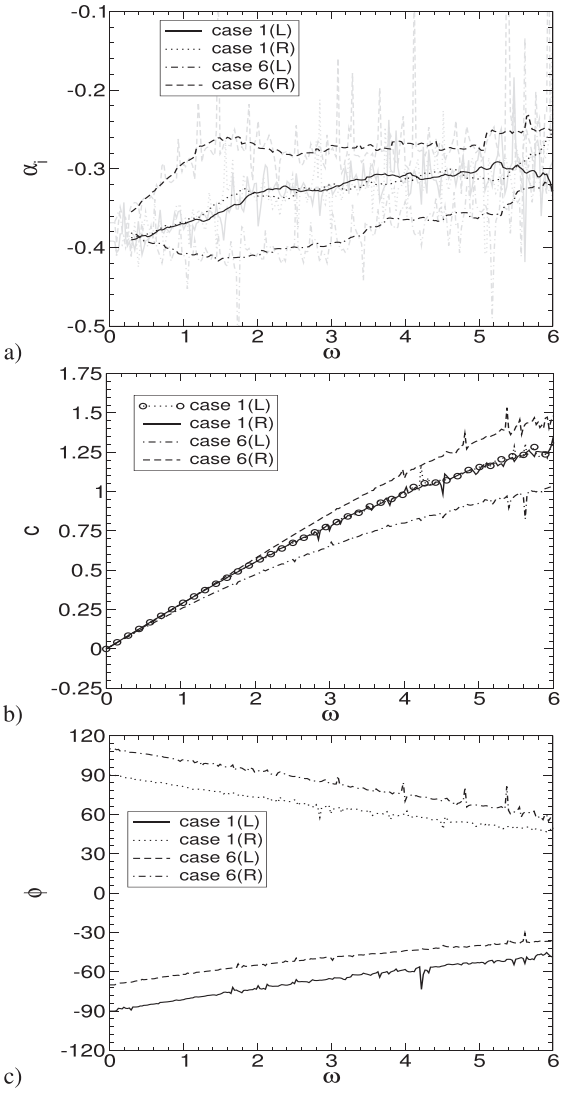

FIG. 24. Comparison of (a) growth rate, (b) phase speed, and (c) wave angle at $s = 12.45$ for radial (case 1) and spiral (case 6) RBP flow and $\beta = 3.43$. For a), gray lines represent raw data and black lines are for data filtered over a frequency interval of $\Delta\omega = 0.612$.

C. Spiral RBP flow-45°

A spiral RBP flow DNS with random forcing was also carried out for a larger inflow angle of 45° (case 7). All other parameters were kept the same as for case 6. The objective was to investigate the dependence of the stability behavior of spiral RBP flow on the inflow angle. Contours of the spatial growth rate for different frequencies and azimuthal wavenumbers for the same three radial locations as for the other cases are displayed in Fig. 26. Overall, for the 45° spiral RBP flow (case 7), the left-traveling waves have higher growth rates and the right-traveling waves have lower growth rates than for the 22.5° case (case 6) as seen in Figs. 23 and 26. Similar to case 6, the growth rate contours of the left- and right-traveling waves are asymmetric with respect to $\beta = 0$ and the growth rates decrease in the streamwise direction. However, compared to case 6, the azimuthal wavenumber range where both families of oblique waves are amplified is narrower for case 7 and the differences between the growth rates for the left- and right-traveling waves are more pronounced. The maximum azimuthal wavenumber for the amplified left-traveling waves is approximately –9 for case 6 (Fig. 23) and almost –6 for case 7 (Fig. 26). The azimuthal wavenumber associated with the most amplified waves is $\beta \approx 2.75$ for case 6 and $\beta \approx 2$ for case 7. Interestingly, not only for the 45° inflow case but also for the 22.5° inflow case, it appears that the unstable regions associated with the left- and right-traveling waves split up into a steady mode and an unsteady mode as seen for example in Figs. 26(b) and 26(c). In Fig. 26(c), the steady modes are roughly located at $\omega = 0$ and $\beta \approx -6, 2$ while the unsteady modes are located at $0.5 \leq \omega \leq 6$ and $\beta \approx -2$ and $2 \leq \omega \leq 8$ and $\beta \approx 4$ (these regions are marked in the figure). This apparent "split up" may indicate the

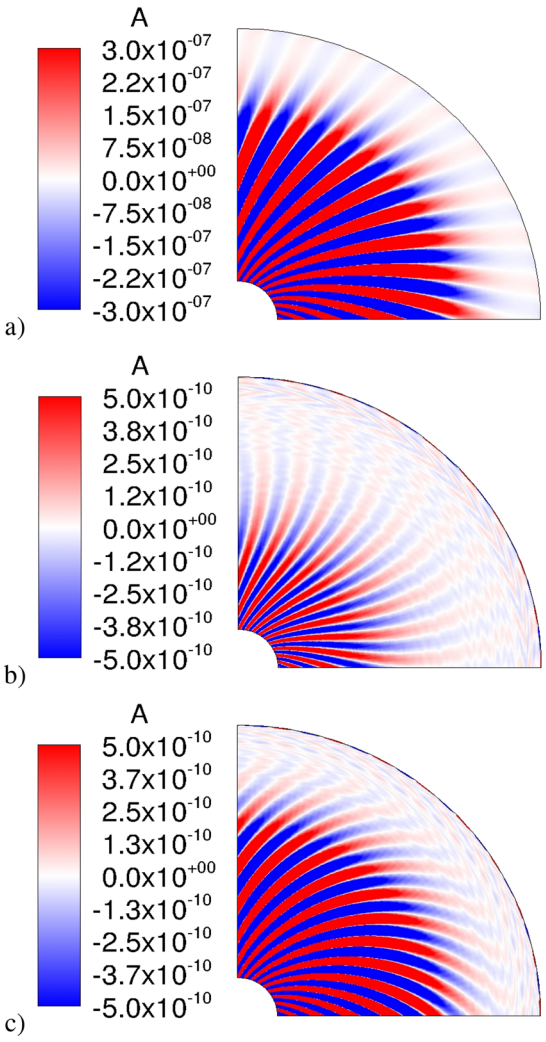

FIG. 25. Iso-contours of wall-normal disturbance velocity amplitude at the channel mid-height for $k = 9$ (case 6): (a) steady waves ($\omega = 0$), (b) right traveling waves ($\omega = 1.227$), and (c) left traveling waves ($\omega = 1.227$).

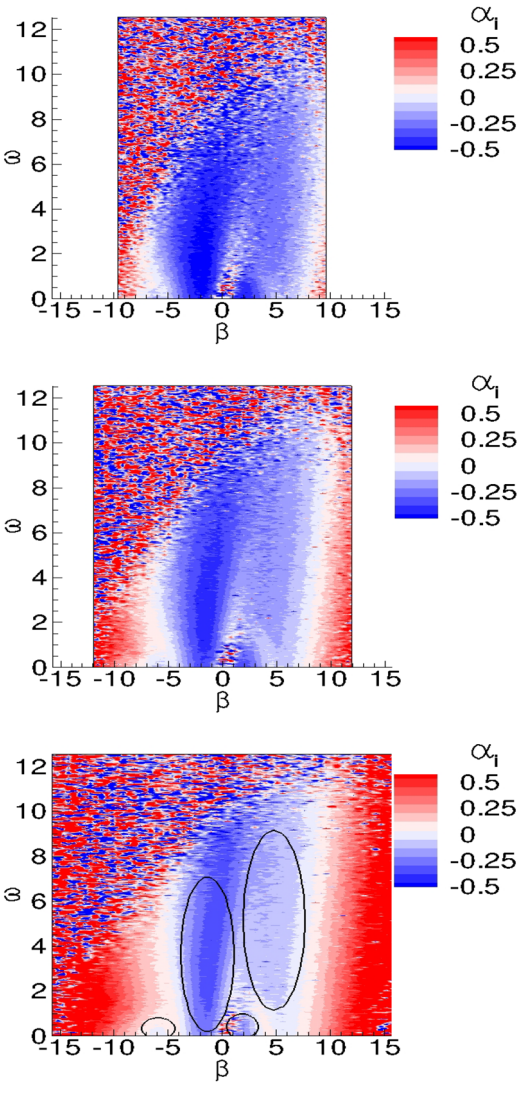

FIG. 26. Contours of the growth rate for (a) $s = 9.96$, (b) $s = 12.45$, and (c) $s = 14.94$ for case 7.

onset of another instability with increasing sweep angle that warrants further analysis.

In Fig. 27, the growth rates, phase speeds, and wave angles at $s = 12.45$ obtained from cases 6 and 7 are compared for $\beta = 3.43$. Figure 27(a) shows that the oblique waves are less amplified for the case with the larger inflow angle (case 7). The phase speeds of the right-traveling waves for the 45° case increase faster with frequency than for the 22.5° case as seen in Fig. 27(b). The left-traveling waves exhibit an opposite tendency. Figure 27(c) shows that the wave angle of the right-traveling waves is increased and the wave angle of the left-traveling waves is decreased for the larger inflow angle.

V. CONCLUSION

The instability of inward radial Rayleigh–Bénard–Poiseuille flow was investigated with direct numerical simulation with random and controlled small (linear in the sense of linear stability theory) amplitude forcing at the inflow. While the instability of plane RBP flow has attracted considerable attention by the scientific community, this is not so much the case for inward radial RBP flow.

Based on the stability diagram in the study by Gage and Reid,[1] a subcritical Reynolds number and supercritical Rayleigh number were chosen for the present analyses. For the inward radial flow with random forcing, steady three-dimensional waves are amplified that merge in the streamwise direction. A wide range of oblique waves are also amplified. However, their growth rates are generally lower than for the steady waves. The azimuthal wavelength of the most amplified steady waves is independent of the radial location and roughly 0.916 times the channel height (channel height, $h = 2$). As the basic flow continues to accelerate toward the outflow, the growth rates are more and more

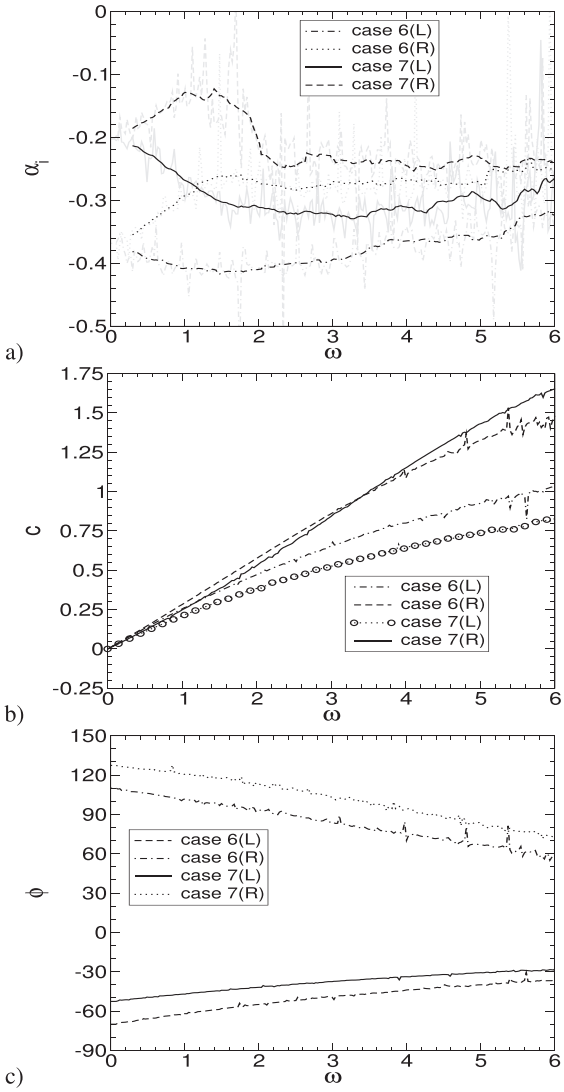

FIG. 27. Comparison of (a) growth rate, (b) phase speed, and (c) wave angle for $\beta = 3.43$ at $s = 12.45$ for cases 6 and 7. In (a), gray lines represent raw data and black lines are for data filtered over a frequency interval of $\Delta\omega = 0.612$.

reduced. The left- and right-traveling oblique waves have very similar growth rates. With increasing frequency, the phase speeds increase and the wave angles decrease. The spatial growth rates obtained from the simulations with controlled inflow forcing are in good agreement with those from the simulation with random forcing. This provides justification for the computationally more efficient simulations with random forcing, which allow for the exploration of a wide parameter space with a single simulation.

Two cases with spiral basic flow were considered as well. The inflow angles for the two cases were 22.5 and 45°. For both cases, the growth rate of one family of oblique waves dominates over the other, and overall, the growth rates and the azimuthal wavenumbers for the strongest amplified oblique waves are lower than those for the radial basic flow. For a fixed azimuthal wavenumber, the left-traveling waves attain higher growth rates and have lower phase speeds and wave angles than for the radial flow case. Similar but opposite observations were made for the right-traveling waves. These trends become more pronounced as the inflow angle is increased.

In summary, the stability of inward radial RBP flow is qualitatively similar to the stability of plane RBP flow. Steady three-dimensional waves are most amplified and may develop into streamwise convection rolls although overall the growth rates are much reduced by the streamwise acceleration. Also different from plane RBP flow, the spanwise wavelength has to be an integer fraction of the circumference, which explains the observed "mergings" steady waves.

The present instability investigation is important for engineering applications that rely on inward radial RBP flows such as the collector of solar chimney power plants. The Rayleigh and Reynolds numbers of the RBP flow in the collector of such plants are much larger than those chosen for the present study. One may, however, argue that the turbulent flow in large collectors may be subject to similar instabilities as those investigated here. Instability could lead to the development of coherent flow structures with potential consequences for the solar chimney power plant performance. For the future, it is planned to simulate the flow through the collector of a 1:33 solar chimney power plant model.[17] The simulations will first be validated by comparison with the experimental measurements. Then, the unsteady data obtained from the simulations will be analyzed using the same post-processing tools and procedures as for the present analysis to uncover and understand the flow instabilities.

ACKNOWLEDGMENTS

This material is based upon the work supported by the National Science Foundation under Grant No. 1510179 with Dr. Ronald Joslin serving as the program manager.

DATA AVAILABILITY

The data that support the findings of this study are available from the corresponding author upon reasonable request.

REFERENCES

[1]K. S. Gage and W. H. Reid, "The stability of thermally stratified plane Poiseuille flow," J. Fluid Mech. **33**, 21–32 (1968).
[2]S. A. Orszag, "Accurate solution of the Orr-Sommerfeld stability equation," J. Fluid Mech. **50**, 689–703 (1971).
[3]J.-M. Luijkx, J. K. Platten, and J. C. Legros, "On the existence of thermoconvective rolls, transverse to a superimposed mean Poiseuille flow," Int. J. Heat Mass Transfer **24**, 1287–1291 (1981).
[4]X. Nicolas, A. Mojtabi, and J. K. Platten, "Two-dimensional numerical analysis of the Poiseuille–Bénard flow in a rectangular channel heated from below," Phys. Fluid **9**, 337–348 (1997).
[5]X. Nicolas, N. Zoueidi, and S. Xin, "Influence of a white noise at channel inlet on the parallel and wavy convective instabilities of Poiseuille–Rayleigh–Bénard flows," Phys. Fluid **24**, 084101 (2012).
[6]K. Fujimura and R. E. Kelly, "Interaction between longitudinal convection rolls and transverse waves in unstably stratified plane Poiseuille flow," Phys. Fluid **7**, 68–79 (1995).
[7]B. S. Ng and W. H. Reid, "Instabilities in plane Poiseuille flow due to the combined effects of stratification and viscosity," Phys. Fluid **9**, 1844–1846 (1997).
[8]Y. Mori and Y. Uchida, "Forced convective heat transfer between horizontal flat plates," Int. J. Heat Mass Transfer **9**, 803–808 (1966).

[9]M. Y. Chang, C. H. Yu, and T. F. Lin, "Changes of longitudinal vortex roll structure in a mixed convective air flow through a horizontal plane channel: An experimental study," Int. J. Heat Mass Transfer **40**, 347–363 (1997).
[10]M. Y. Chang and T. F. Lin, "Experimental study of aspect ratio effects on longitudinal vortex flow in mixed convection of air in a horizontal rectangular duct," Int. J. Heat Mass Transfer **41**, 719–733 (1998).
[11]S. Mergui, X. Nicolas, and S. Hirata, "Sidewall and thermal boundary condition effects on the evolution of longitudinal rolls in Rayleigh-Bénard-Poiseuille convection," Phys. Fluid **23**, 084101 (2011).
[12]M. K. Hasan and A. Gross, "Higher–order–accurate numerical method for temporal stability simulations of Rayleigh–Bénard–Poiseuille flows," Int. J. Numer. Methods Fluids **93**, 127–147 (2021).
[13]M. K. Hasan and A. Gross, "Temporal secondary stability simulation of Rayleigh-Bénard-Poiseuille flow," Int. J. Heat Mass Transfer **159**, 120098 (2020).
[14]H. L. Reed and W. S. Saric, "Linear stability theory applied to boundary layers," Annu. Rev. Fluid Mech. **28**, 389–428 (1996).
[15]H. Fasel, F. Meng, E. Shams, and A. Gross, "CFD analysis for solar chimney power plants," Sol. Energy **98**, 12–22 (2013).
[16]H. F. Fasel, F. Meng, and A. Gross, "Numerical and experimental investigation of 1:33 scale solar chimney power plant," in 11th International Conference on Heat Transfer, Fluid Mechanics, and Thermodynamics (2015).
[17]M. K. Hasan, A. Gross, L. Bahrainirad, and H. F. Fasel, "Numerical investigation of flow inside the collector of a solar chimney power plant," in AIAA Scitech 2021 Forum (2021).
[18]M. A. D. S. Bernardes, R. M. Valle, and M. F. B. Cortez, "Numerical analysis of natural laminar convection in a radial solar heater," Int. J. Therm. Sci. **38**, 42–50 (1999).
[19]M. A. D. S. Bernardes, "Preliminary stability analysis of the convective symmetric converging flow between two nearly parallel stationary disks similar to a solar updraft power plant collector," Sol. Energy **141**, 297–302 (2017).
[20]M. A. D. S. Bernardes, "Correlations for the symmetric converging flow and heat transfer between two nearly parallel stationary disks similar to a solar updraft power plant collector," Sol. Energy **146**, 309–318 (2017).
[21]H. Van Santen, C. R. Kleijn, and H. E. A. Van Den Akker, "Mixed convection in radial flow between horizontal plates-I. Numerical simulations," Int. J. Heat Mass Transfer **43**, 1523–1535 (2000).
[22]H. Van Santen, C. R. Kleijn, and H. E. A. Van Den Akker, "Mixed convection in radial flow between horizontal plates-II. Experiments," Int. J. Heat Mass Transfer **43**, 1537–1546 (2000).
[23]A. Singh, B. D. Vyas, and U. S. Powle, "Investigations on inward flow between two stationary parallel disks," Int. J. Heat Fluid Flow **20**, 395–401 (1999).
[24]R. D. Sandberg, "Governing equations for a new compressible Navier-Stokes solver in general cylindrical coordinates," Technical Report No. AFM-07/07 (University of Southampton, Southampton, UK, 2007).
[25]E. A. Spiegel and G. Veronis, "On the Boussinesq approximation for a compressible fluid," Astrophys. J. **131**, 442–447 (1960).
[26]P. Fan, "The standard upwind compact difference schemes for incompressible flow simulations," J. Comput. Phys. **322**, 74–112 (2016).
[27]R. K. Shukla, M. Tatineni, and X. Zhong, "Very high-order compact finite difference schemes on non-uniform grids for incompressible Navier-Stokes equations," J. Comput. Phys. **224**, 1064–1094 (2007).
[28]D. J. Fyfe, "Economical evaluation of Runge-Kutta formulae," Math. Comput. **20**, 392–398 (1966).
[29]J.-R. Carlson, "Inflow/outflow boundary conditions with application to FUN3D," Report No. NASA/TM-2011-217181 (NASA Center for AeroSpace Information, Hanover, MD, 2011).
[30]A. Gross and H. F. Fasel, "Characteristic ghost cell boundary condition," AIAA J. **45**, 302–306 (2007).